Available online at www.sciencedirect.com
ScienceDirect
Journal of Sound and Vibration 315 (2008) 279–300
JOURNAL OF SOUND AND VIBRATION
www.elsevier.com/locate/jsvi

Effect of discrete track support by sleepers on rail corrugation at a curved track

X.S. Jin*, Z.F. Wen

State Key Laboratory of Traction Power, Southwest Jiaotong University, Chengdu 610031, China

Received 15 September 2007; received in revised form 20 December 2007; accepted 19 January 2008
Handling Editor: L.G. Tham
Available online 10 March 2008

Abstract

The paper investigates into the effect of discrete track support by sleepers on the initiation and development of rail corrugation at a curved track when a railway vehicle passes through using a numerical method. The numerical method considers a combination of Kalker's rolling contact theory with non-Hertzian form, a linear frictional work model and a dynamics model of a half railway vehicle coupled with the curved track. The half-vehicle has a two-axle bogie and doubled suspension systems. It is treated as a full dynamic rigid multi-body model. In the track model, an Euler beam is used to model the rail, and the discrete track support by sleepers moving backward with respect to the vehicle running direction is considered to simulate the effect of the discrete sleeper support on the wheels/rails in rolling contact when the vehicle moves on the track. The sleeper is treated as a rigid body and the ballast bed is replaced with equivalent mass bodies. The numerical analysis exams in detail the variations of wheel/rail normal loads, the creepages, and the rail wear volume along the curved track. Their variations are much concerned with the discrete track support. The numerical results show that the discrete track support causes the fluctuating of the normal loads and creepages at a few frequencies. These frequencies comprise the passing frequency of the sleepers and the excited track resonant frequencies, which are higher than the sleeper passing frequency. Consequently, rail corrugation with several wavelengths initiates and develops. Also the results show that the contact vibrating between the curved rails and the four wheels of the same bogie has different frequencies. In this way, the different key frequencies to be excited play an important role in the initiation and development of curved rail corrugation. Therefore, the corrugations caused by the four wheels of the same bogie present different wavelengths. The paper shows and discusses the depths of the initial corrugations caused by the four wheels of the same bogie, at the entering transition curve, the circle curve and the exit transition curve of the curved track, respectively.

1. Introduction

After use of new railway tracks corrugations more or less appear soon due to irregularities of the tracks. One of track irregularities is the discrete track support by sleepers. According to site observations and studies in many published papers it was found that the discrete track support is a key factor causing rail corrugation. In the 1980s of last century, Clark found that the short wavelength corrugation occurred only in the second

*Corresponding author. Tel.: +86 28 87634355; fax: +86 28 87600868.
E-mail address: xsjin@home.swjtu.edu.cn (X.S. Jin).

0022-460X/$ - see front matter © 2008 Elsevier Ltd. All rights reserved.
doi:10.1016/j.jsv.2008.01.057

half of each sleeper bay, on high speed sections on British Railway [1]. Through theoretical analysis he also found that the normal force of wheel–rail in rolling contact oscillates at corrugation passing frequency on either sides of the wheel–rail static load, and the oscillation amplitude is greatest near sleeper positions [2]. Ref. [3] analyzed the conditions necessary for the existence in the British Rail system of corrugations ranged in 40–80 mm with two oscillators in reference to track discrete support structure, friction and locomotive traction characteristics. The frequency characteristics of the two oscillators cover corrugation wavelength range of 38–89 mm, which is in substantial agreement with British observations. Such a type of rail corrugation was referred to as roaring rail corrugation by Grassie and Kalousek [4], and attributed to wear mechanism and the concerned factors including vertical dynamic loads, creepages between wheel and rail. Usually, the misalignment and rolling-slip of wheelsets occur when the wheelsets hunt at a tangent track, the lateral and longitudinal creepages between the wheels and rails become larger. It can be predicted that the larger conformity and contact angle between wheel and rail leads to the larger spin creepage and the severe wear between them.

Ahlbeck and Daniels [5] discussed the basic differences and characteristics of long wavelength (heavy haul) and short wavelength (transit/passenger) corrugations, based on their review of corrugation literatures. They concluded that transit/passenger corrugations show characteristic grouping in their development. These short wavelength corrugations mainly grouped in the second half sleeper bay and near the peak of wheelset kinematical hunting.

Knothe and his group made a detailed investigation into the material wear situation at the different positions in a sleeper bay with the concepts of receptance and pinned–pinned mode [6,7], and found that high corrugation growth rate sets in the position of the rail over a sleeper.

Vadillo and his colleagues found that the about 60 mm wavelength corrugation appeared at the mid-span of each sleeper bay with 1000 mm size in the Bilbao area, Spain. Through the test in which an intermediate sleeper was inserted in between each two sleepers with 1000 mm size the corrugations were ceased [8]. To further explain the rare behavior they observed, Gomez and Vadillo [9] utilized the linear model for corrugation developed by Frederick to analyze it, and demonstrated that a corrugation initially presented at the mid-span and almost disappeared above the sleeper.

Jin et al. [10] investigated the effect of track irregularities on initiation and evolution of rail corrugation. In their study the effect of periodical variation of sleeper support on rail corrugation on the curved track was analyzed by inputting a vertical track irregularity due to the periodically passing of sleepers. The vertical flexibility variation of track, due to the discrete sleeper support, was predicted by finite element method in the static state of wheel in contacting with rail. The corrugation model presented in Ref. [10] considered a vertical coupling dynamical behavior of a curved track and a single wheel with a single suspension system supporting a mass body. Obviously using such a model neglects the fact that multiple wheel/rail interactions occur when a train passes over the track. In recent study of wheel/rail noise generation, Wu and Thompson [11] found that the wheel/rail force spectrum had several peaks at different frequencies due to the wave reflection between the wheels on a rail. They investigated the normal force behavior, much concerned with rail corrugation wavelengths, under multiple wheel/rail interaction [12]. They also analyzed the formation of short pitch rail corrugation using an approach combining wheel/track dynamics, contact mechanics and wear, in which multiple wheel/rail interactions were taken into account in the wheel/track dynamics [13].

Recently, Jin et al. [14,15] developed a three-dimensional (3D) train–track model for study of rail corrugation in time domain. This model took the vertical and lateral coupling dynamics of a half passenger car and a curved track into account. The crossing influence of the four wheels of a bogie, or the interaction of the leading and trailing wheelsets, on rail corrugation was taken into consideration. In Refs. [14,15], the natural frequency characters of the track model were investigated in detail. It was found that the track model of Euler beam presented the symmetrical and unsymmetrical pin–pin modes (or frequencies) of the track, in the vertical and lateral directions. According to vibration theory, not all the natural frequencies of track structure, including the pin–pin frequencies, can be excited under wheels. If the pin–pin frequency is not activated, it does not play a part in the corrugation formation. In the opinion of the present authors, the passing frequency of track sleepers is one of the key factors influencing rail corrugation wavelength. The passing frequency of track sleepers is determined by the sleeper distance and the vehicle speed. So, it is essential to develop theoretical models of vehicle and track in time domain [16–18], to investigate the effect of sleeper passing

frequency on rail corrugation in detail. In the time domain theoretical models, if the vehicle with respect to the track, or the track with respect to the vehicle is assumed to be in a static state, such models cannot characterize the effect of track discrete support by sleepers on rail corrugation.

The corrugation models in Refs. [10,14,15] neglect the effect of track discrete support on rail corrugation directly. Namely, in the calculation of the coupling dynamics of the vehicle and the track with the models, the track is assumed to be in a static state with respect to the vehicle. Ref. [15] in detail investigated the effect of passenger car curving on the corrugation initiation at a curved track. Since the corrugation model neglected the effect of discrete sleeper support moving with respect to the running vehicle and the other track irregularities on the dynamical behavior of the vehicle and track, the high-frequency contact vibrating attenuated with the passage increasing of the vehicle. The short pitch corrugation of about 30 mm caused by the leading wheelset gradually leveled out and long wavelength corrugation of about 580–600 mm generated (see Fig. 13 in Ref. [15]). However, the trailing wheelset caused nearly uniform wear on the rail running surfaces (see Fig. 14 in Ref. [15]), namely, no contact vibration occurred or very slight contact vibration occurred between the trailing wheelset and the curved rails when the vehicle passes through the ideal curved track. At that time the authors could not make sure that the reason for the corrugation generation with 580–600 mm wavelength was just related to the excitation of the passing sleepers with 600 mm pitch because the calculation model used in Ref. [15] assumed that the discrete support by sleepers were in static state with respect to the running vehicle. The excitation of the discrete support by sleepers to the vehicle/track system was neglected. Hence, the models used in Refs. [14,15] cannot character the effect of the discrete sleeper support moving with respect to the running vehicle on initiation and development of curved rail corrugation. Ref. [19] developed the track model with moving discrete support to investigate the short pitch corrugation formation on the tangent track when the vehicle is hunting. It was found that short pitch wear-type corrugation occurs on the tangent track where the maximum peaks of the wheelset yaw angle appear under the wheelset hunting. In the present study, the corrugation model in Ref. [19] is used to investigate the effect of sleeper pitch on the corrugation formation on a curved track without vehicle hunting.

2. Calculation model of rail corrugation

2.1. General descriptions for rail corrugation model

Characteristics of rail corrugation, such as wavelength, wave-depth, metallurgical aspects, etc., depend greatly on the profiles and material properties of wheel and rail, train speed, and the dynamical characteristics of railway vehicle and track. Therefore, it is essential to develop a comprehensive model accounting for more concerned factors affecting rail corrugation to predict the initiation and development of rail corrugation accurately. The present model is roughly depicted in Fig. 1. In Fig. 1 Y_{wi} and ψ_{wi} are, respectively, the lateral displacement and the yaw angle of wheelset i, subscript i denotes the number of the wheelset considered in the calculation model, Y_{rk} is the lateral displacement of the rail head under wheel k, and subscript k is the number of the wheel, δ_k and h_k are, respectively, the contact angle and the normal distance between wheel k and the rail. The selected ranges for i and k depend on the total number of the wheelsets or the wheels in the calculation model. ξ_{jk} and P_{wrzk} are, respectively, the creepage and the vertical load between the wheel and the rail, subscripts $j = 1$–3 indicate, respectively, the longitudinal, lateral and spin creepages of the wheel and rail, subscripts w and r denote, respectively, the wheel and the rail, z indicates the vertical direction of the track. f_{wk} denotes the frictional work density in the contact area under wheel k. Fig. 1 indicates a feed-back process between the transient coupling dynamics of railway vehicle and track and the long-term wear processes. In the calculation of rail corrugation at a curved track, a coupling dynamics model of a half-vehicle and a curved track is used to analyze the dynamical behavior of the vehicle passing over the curved track. Through the dynamics analysis, ξ_{jk}, P_{wrzk} Y_{wi}, ψ_{wi} and Y_{rk} are obtained. According to Y_{wi}, ψ_{wi} and Y_{rk}, using the calculation method for wheel–rail contact geometry [20] calculates h_k and δ_k. ξ_{jk}, P_{wrzk}, h_k and δ_k are used in calculating the rolling contact mechanics of the wheel/rail, in which Kalker's model of 3D elastic bodies in rolling contact is introduced and slightly modified to calculate f_{wk}, contact stresses, stick/slip areas, etc. [14,15,19]. The frictional work density in the contact area is calculated by using the tangent traction components and the total slip components between a pair of the contacting particles in the contact

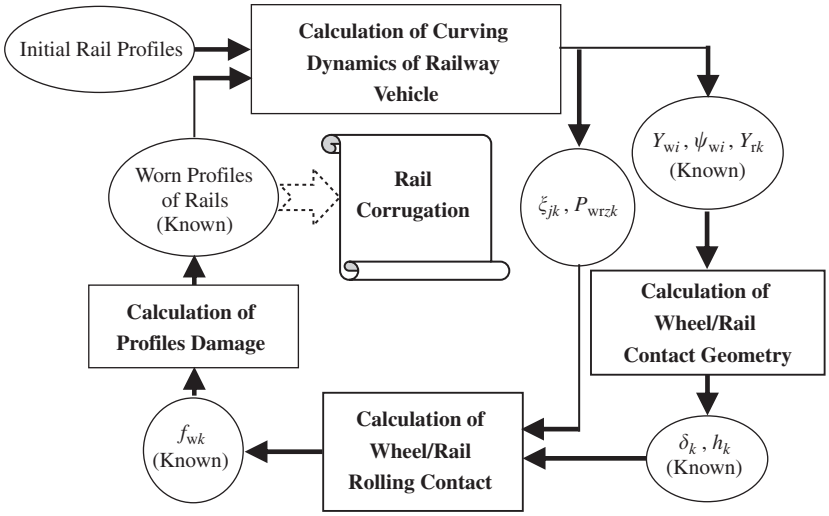

Fig. 1. A general description of curved rail wear model.

area. The undulatory wear depth on the rail running surface is determined with the material wear model by Clayton et al. In the wear model the material loss of unit area is assumed to be proportional to the frictional work density [21–23]. Using the known wear depth at the present step updates the existing rail profile for the next loop calculation. After the repeated loop calculations the accumulated material wear and its pattern on the rail head exhibit. It should be pointed out that, for the introduced rail wear model, the effect of material work hardening, due to repeated rolling and press of wheels, on the wear is neglected.

2.2. Model of railway vehicle and curved track

At railway sites, severe corrugations, usually, occur at curved tracks, as shown in Figs. 2(a) and (b). Fig. 2(a) presents rail corrugation wavelengths of 2.8–3.2 m on the low rail of the curved track with a radius of 800 m and the average running speed of 120 km/h in the passenger track, and Fig. 2(b) shows 200–300 mm wavelengths of high rail corrugation on the curved track with radius of 600 m in the heavy haul line. So far in explanation for the mechanism of such corrugations occurred on curved tracks there has not been an available 3D model considering the effect of the discrete rail support in time domain.

The present model considers a half-vehicle and a curved track with $1435+2$ mm gauge and 300 m radius. The rail cant is $\alpha_t = 1/40$, and the sleeper pitch $l_s = 600$ mm. It is assumed that each passage of the half-vehicle is at constant speed, $v = 80$ km/h.

The calculation model of the half-vehicle coupled with the track is described with Figs. 3(a) and (b). In the figures, the subscript z of some parameters indicates the vertical direction of the system, y indicates the lateral direction, and x the forward direction of the vehicle. From Fig. 3 it is obvious that the half-vehicle is treated as a full dynamic rigid multi-body model. The track, except for the rails, is also treated as a dynamic rigid multi-body model. Each rail is replaced with an Euler beam characterizing the vertical, lateral and rotational deformations of the rail. It should be noted that the calculation model of the rail support, as shown in Fig. 3(b), is slightly different from that in Refs. [14,15], namely, in the longitudinal and vertical plane of the track, the rail restriction for the rail pitch motion by the track structure under the rail is taken into consideration. A linear rotational spring K_{rt}, a linear vertical spring K_{rz} and a vertical damper K_{cz} are used to equivalently replace the fastening system, as shown in Fig. 3(b).

In order to present the motion equations of the system and the numerical results clearly and conveniently, the left wheel and the right one of the leading wheelset are numbered 1 and 2, respectively, and the corresponding wheels of the trailing wheelset numbered 3 and 4. The leading and trailing wheelsets are numbered 1 and 2, respectively. In Fig. 3, subscript θ indicates the pitching angle of the parts of the system, ϕ indicates the rolling angle, P_{wrzk} ($k = 1$–4) indicate the vertical loads between the four wheels and the rails,

Fig. 2. (a) Long pitch corrugation on low curved rail at 120 km/h and (b) medium pitch corrugation on high curved rail at 80 km/h.

C and K with subscripts stand for the coefficients of the equivalent dampers and those of stiffness of the equivalent springs, respectively. The equivalent dampers and springs are used to replace the connection between the components of the vehicle and track, as shown in Fig. 3. It should be noted that since the half-vehicle is considered in the dynamics analysis it cannot be balanced when it is running on the track. Therefore, the pitching and yaw motions of the carriage have to be neglected, namely, let $\psi_c = 0$, as shown in Fig. 3(a), and $\theta_c = 0$, as shown in Fig. 3(b).

2.2.1. *Motion equations of vehicle and track*

The considered system contains many differential equations and the detailed derivation of the equations is tedious. The equations were given directly, and their symbols were explained in Refs. [14,15]. The present paper emphasizes the discussion on the improved track model and the corresponding differential equations.

The calculation model of the track used in Ref. [24] is modified and used in the present paper. Considering the half-vehicle passing through the track, only the four wheels of the same bogie interact with the two rails. Each rail is modeled by Euler beam. The calculation model of the wheels coupled with the beam is illustrated with Fig. 4. The calculation length of the beam $l_{er} = 36$ m, and the two ends of the beam are hinged. $x_{w1(2)}$ and $x_{w3(2)}$ are the distances from the beam end A to wheel 1(2) and wheel 3(4), respectively. The center of the bogie is set on the center of the rail (beam). x_{si} is the distance from the end A to sleeper i. In order to simulate the effect of the discrete sleeper support on the coupling dynamics of the vehicle and the track when the vehicle running at constant speed v, the sleepers under the beam are assumed to move backward at the same speed,

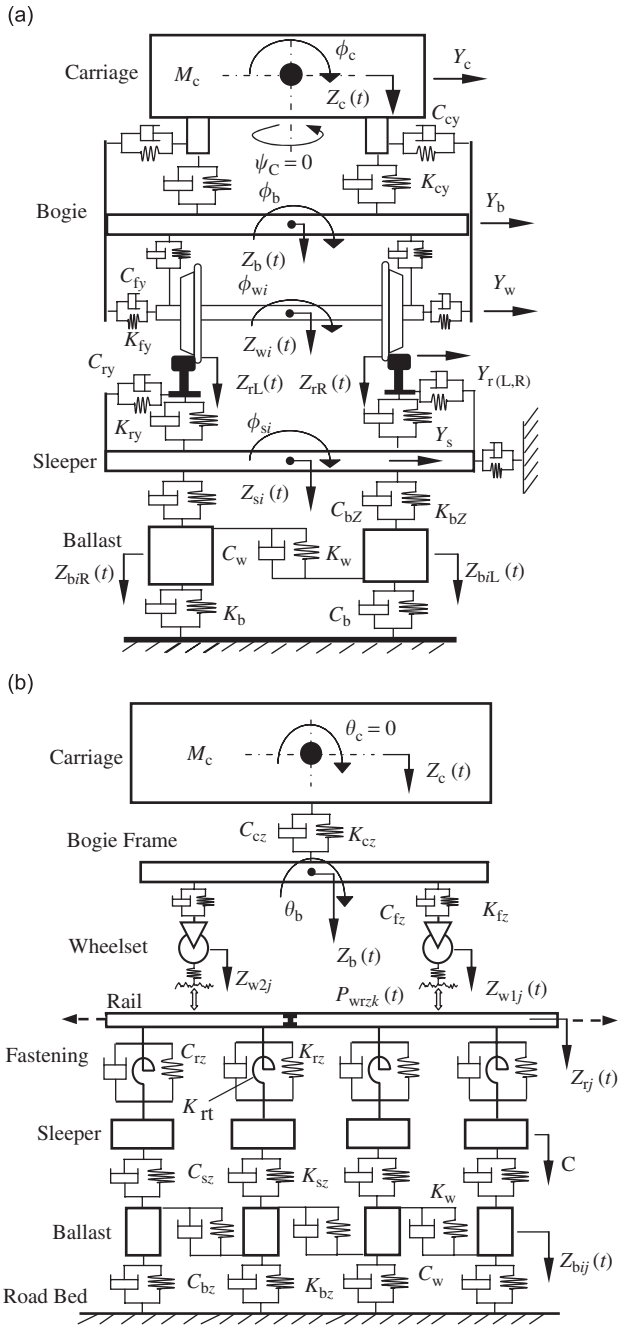

Fig. 3. (a) Elevation of a half passenger car coupled with a curved track and (b) side elevation.

and the vehicle is static with respect to the beam. When the sleepers (1 to $i+1$), as shown in Fig. 4, start to move backward, the sleeper $i+2$ appears from the end B. Before sleeper 1 reaches the end A the beam is supported by the sleepers of $i+2$. After sleeper 1 disappears at the end A, the sleepers of $i+1$ support the beam, being the same as the initial state. The same process is repeated. The behavior of the discrete support by sleepers presents a periodical action on the beam. The period is $T_s = l_s/v$. The action pattern seems to be like a track section with length l_{er} moves with the vehicle running at speed v. The sleeper enters from the end B and leaves from the end A. The beam ends A and B are hinged, and are regarded as the moving ends. The present

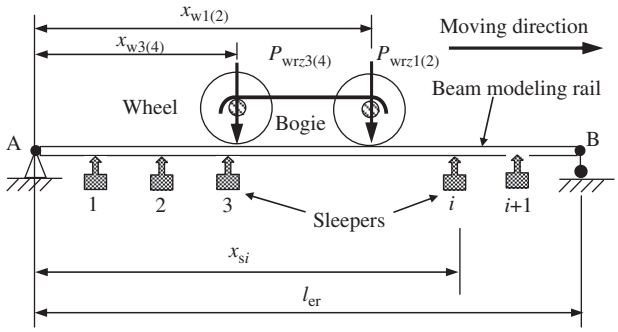

Fig. 4. Calculation model of wheels and rail interaction.

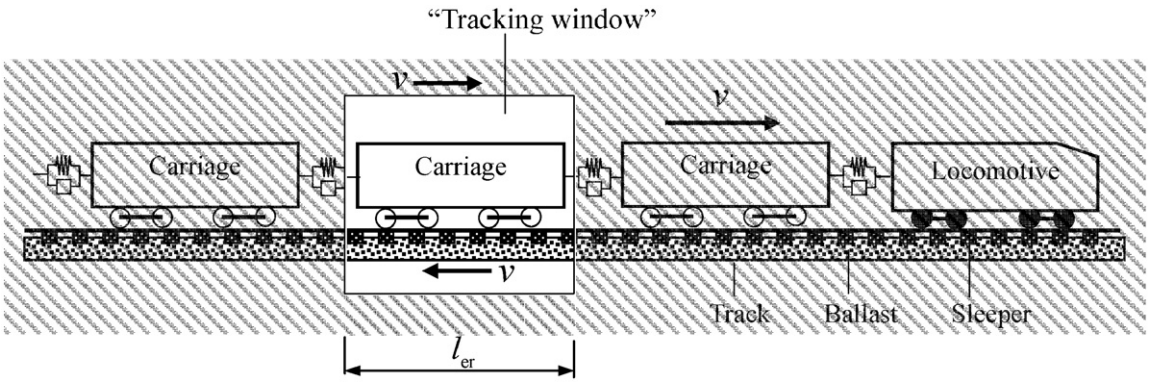

Fig. 5. Calculation model of the moving track discrete support.

coupling model of the vehicle and the track seems that one watches the behavior of the vehicle running along the track through a window with l_{er} width. The window moves forward at the speed of the vehicle. The vehicle is statically in the window. The track passes through the window in the inverse direction, at the speed of the vehicle, as shown in Fig. 5.

In order to eliminate the effect of the hinged ends of the beam, the value of l_{er} is much longer than the wheelbase of the bogie. l_{er} is selected to be 36 m which covers 60 sleeper bays, namely 59 or 60 sleepers. x_{si} is written as

$$\begin{cases} x_{s1} = l_s - vt & (0 \leqslant t \leqslant T_s = l_s/v) \\ x_{s2} = 2l_s - vt & (0 \leqslant t \leqslant 2T_s = 2l_s/v) \\ \cdots\cdots & \\ x_{si} = il_s - vt & (0 \leqslant t \leqslant iT_s = il_s/v) \end{cases}. \tag{1}$$

The rail restriction by the fastening system in the longitudinal and vertical plane of the track is replaced with a vertical linear spring of stiffness K_{rc}, a linear rotational spring K_{rt} and a vertical linear damper C_{rz}, as shown in Fig. 6. In the lateral and vertical plane of the track, the rail restriction by the fastening systems was discussed in detail [14,15]. The coordinate of each sleeper is a constant, denoted by x_{Fi} in Ref. [15]. The vertical and lateral bending deformations and rotation of the rails are taken into account. The longitudinal deformation and the crossing influence of the vertical and lateral bending and rotational deformations of the rails are ignored. Using the Rayleigh–Ritz method the fourth-order partial differential equations of the rail are converted into second-order ordinary equations as follows:

$$\ddot{q}_{zk}(t) + \frac{EI_y}{m_r}\left(\frac{k\pi}{l}\right)^4 q_{zk}(t) = -\sum_{i=1}^{N}[F_{zi}Z_k(x_{si}) + M_{sti}Z'_k(x_{si})] + \sum_{j=1,3 \text{ or } 2,4} F_{wrzj}Z_k(x_{wj}), \tag{2}$$

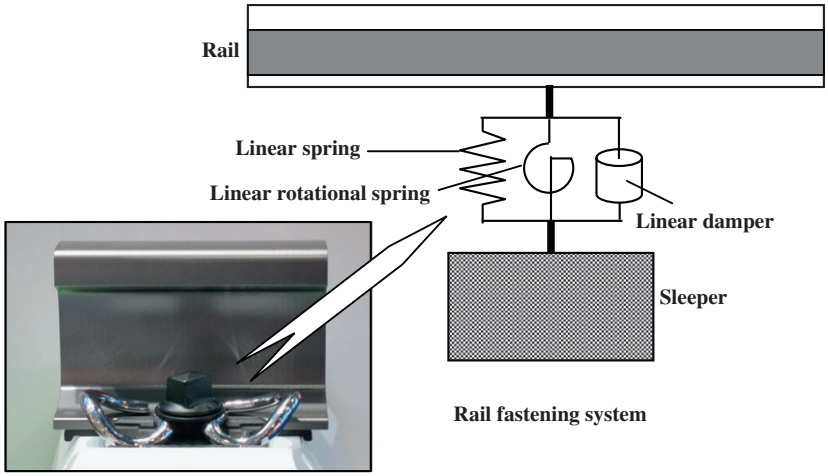

Fig. 6. Calculation model of fastening system in longitudinal and vertical plane of track.

$$\ddot{q}_{yk}(t)+\frac{EI_z}{m_r}\left(\frac{k\pi}{l}\right)^4 q_{yk}(t)=-\sum_{i=1}^{N}F_{yi}\,Y_k(x_{si})+\sum_{j=1,3\text{ or }2,4}F_{wryj}\,Y_k(x_{wj}), \tag{3}$$

$$\ddot{q}_{Tk}(t)+\frac{GK}{\rho I_0}\left(\frac{k\pi}{l}\right)^2 q_{Tk}(t)=-\sum_{i=1}^{N}M_{si}\Theta_k(x_{si})+\sum_{j=1,3\text{ or }2,4}M_{wj}\Theta_k(x_{wj}). \tag{4}$$

Eqs. (2)–(4) are, respectively, the vertical, lateral and rotational equations of motion. $q_{zk}(t)$, $q_{yk}(t)$ and $q_{Tk}(t)$ are the generalized coordinates, and describe the vertical, lateral and rotational motions of the rail, EI_y, EI_z and GK are the vertical bending, lateral bending and rotational stiffness of the rail, E is Young's modules, m_r is the mass per unit longitudinal length, I_0 is the radial second area moment of the rail, ρ is the density of the rail material, $Z_k(\cdots)$, $Y_k(\cdots)$ and $\Theta_k(\cdots)$ are the kth mode functions of the rail in vertical bending, lateral bending, and rotation, $Z'_k(\cdots)$ is the derivative of $Z_k(\cdots)$ with respect to the sleeper coordinate describing the sleeper location on the beam. In the equations subscript $k=1,2,3,\ldots,120$. 120 is the total number of the rail mode functions selected in the calculation. Ref. [25] made an investigation on the effect of the number of beam mode functions used in the expression for the rail motion on the numerical results, and suggested that the selected number of beam mode functions should be larger than 60. The best selection is 90. The authors of the present paper also analyzed the effect of the different numbers of the mode functions on the simulation results. It was found that there was no great difference between the numerical results for the mode functions of 60–120 used in the calculation. If the number of the rail mode function was larger than 120 the calculation was very time-consuming. If the number was larger than 150, the numerical method hired in the present paper was not convergent. For the number of 120 used in the present paper, the represented maximum frequency of the rail should reach about 3700 Hz using the beam theory. But such high frequency of the rail was not excited by the passing wheelsets. $N=59$ or 60, the number of the sleepers shown in Fig. 4, which depend on the location of the moving sleepers under the beam. F_{zi} and F_{yi} are, respectively, the vertical and lateral supporting forces of the rail by sleeper i, M_{sti} is the moment on the rail by the equivalent rotational spring K_{rt}, as shown in Figs. 3(b) and 6, F_{wrzj} and F_{wryj} are the vertical and lateral forces between wheel j and the corresponding rail. It is noted that Eqs. (2)–(4) with subscript $j=1$, 3 or 2, 4 stand for the equations of the left and right rails, respectively. From Eqs. (2) to (3), it is obvious that an interaction of the two axles of the bogie on the rails can be taken into account in the wear analysis. In Eq. (4), M_{si} and M_{wj} are the equivalent calculated moments on the rail, and were discussed in Refs. [14,15]. The vertical motion equation of the rail in Refs. [14,15] does not include M_{sti} by the fastening system, and x_{si} is constant. Therefore, the track model used in Refs. [14,15] is further improved in the present paper.

Through the dynamic calculation, $q_{zk}(t)$, $q_{yk}(t)$ and $q_{Tk}(t)$ are obtained. Therefore, the vertical, lateral and rotational displacements of the rail are written, based on the superposition principle of beam theory, as

$$Z_r(x,t)=\sum_{k=1}^{120} Z_k(x)q_{zk}(t), \quad Y_r(x,t)=\sum_{k=1}^{120} Y_k(x)q_{yk}(t), \quad \phi_r(x,t)=\sum_{k=1}^{120} \Theta_k(x)q_{Tk}(t). \tag{5}$$

The sleeper is represented by a rigid rectangular beam in the calculation model. Only the vertical, lateral and rolling motions of it are considered. To date it is very difficult completely to characterize ballast bed with any existing mathematical model. The calculation model of ballast bed in Ref. [24] is discussed in Ref. [14], as shown in Fig. 3, and introduced in the present study. Only the vertical motion of the ballast bodies is taken into consideration. The motion of the subgrade is neglected.

2.2.2. Model of wheel–rail contact

In the analysis of the transient coupling dynamics of the vehicle and curved track, it is necessary that an accurate and quick calculation model of wheel–rail coupling system is used. The calculation model of wheel–rail coupling, usually, includes the normal and tangential contact problems. The normal load of the wheel–rail, considering the influence of the wear of rail running surface, is approximately described with a Hertzian contact spring with a unilateral restraint, discussed in Refs. [14,15]. Shen–Hedrick–Elkins' model is adopted as the calculation model of the tangential forces between the wheels and rails [26]. Shen–Hedrick–Elkins' model was developed based on Kalker's linear creep theory [27] and the nonlinear creep theory by Vermulen–Johnson's [28]. The model by Shen et al. is a simple mathematical model and very fast in determining the total creep forces.

2.2.3. Initial and boundary conditions of track and vehicle

Due to the two hinged ends of the Euler beam modeling the rails, the deflections and the bending moments at the beam ends are zero. The initial displacements and velocities of all parts of the vehicle are set to be zero in the vertical and lateral directions. The track discrete support comprising the fastening system, the sleepers, and the ballast bodies has the backward motion at the vehicle curving speed. The motion of the road bed is neglected. The vertical motion of the two ends of the considered ballast bed is assumed to be always zero. The curving speed, related to the centrifugal inertial force of the curving vehicle, is included in the differential equations of the vehicle.

Zhai et al. [24] developed a numerical method specifically to solve the coupled dynamic equations of the railway vehicle and track. The stability, calculation speed and accuracy of the numerical method for solving the system equations were also discussed in detail. The coupling dynamics modal of the vehicle and the track and its numerical method were verified by the tests at the railway sites [29,30].

The values of concerned parameters of the vehicle and the track used in the dynamics calculation are listed in Table 1. In Table 1 subscripts x, y and z stand for the longitudinal, lateral and vertical directions, respectively; M_c, M_t, M_w, M_s, and M_b are the masses of the car-body, the bogie, the wheelset, the sleeper and the ballast body, respectively; I_{cx} is the initial moment of the car-body in roll; I_{tx}, I_{ty} and I_{tz} are the moments of inertia of the bogie in roll, pitch and yaw; I_{wx}, I_{wy} and I_{wz} are the moments of inertia of the wheelset in roll, pitch and yaw; C with subscripts indicates the damping coefficient of the equivalent springs, as shown in Fig. 3, and K with subscripts denotes stiffness coefficient of the equivalent springs. The other symbols in Table 1 were previously explained in the text.

The stiffness coefficient K_{rt} of the equivalent linear rotational spring is predicted. It is assumed to be 20,000 N m/rad. So far it is difficult to obtain its accurate value by experiment. Through the numerical investigation it is found that the K_{rt} variation within a certain range has an influence on the amplitude of the rail vibrating in the vertical direction at passing frequency of the sleepers. The too large selected value of K_{rt} causes the divergence of the present numerical procedure. If K_{rt} is less than 15,000 N m/rad, its influences on the vertical bending vibration of the rail is very small. The effect of the different values of the track structure parameters on rail corrugation will be in detail investigated in the near future.

Table 1
Parameters of structures of passenger car and track

Parameter	Value	Parameter	Value	Parameter	Value
M_c (kg)	1.7×10^4	K_{fy} (MN/m)	5	C_{ry} (N s/m)	5.0×10^4
M_t (kg)	3.0×10^3	K_{fz} (MN/m)	0.55	C_{rz} (N s/m)	5.0×10^4
M_w (kg)	1.4×10^3	C_{cy} (kN s/m)	60	K_{rt}(N m/rad)	2.0×10^4
I_{cx} (kg m^2)	3.8×10^4	C_{cz} (kN s/m)	80	K_{sy} (N/m)	3.0×10^7
I_{tx} (kg m^2)	2.26×10^3	C_{fz} (kN s/m)	6	K_{sz} (N/m)	7.0×10^7
I_{ty} (kg m^2)	2.71×10^3	m_r (kg/m)	60.64	C_{sy} (N s/m)	6.0×10^4
I_{tz} (kg m^2)	3.16×10^3	I_0 (m^4)	3.741×10^{-5}	C_{sz} (N s/m)	6.0×10^4
I_{wx} (kg m^2)	915	I_y (m^4)	3.217×10^{-5}	K_w (N/m)	7.8×10^7
I_{wy} (kg m^2)	140	I_z (m^4)	5.24×10^{-6}	C_w (N s/m)	8.0×10^4
I_{wz} (kg m^2)	915	ρ(kg/m^3)	7.8×10^3	K_{bz} (N/m)	6.5×10^7
K_{cx} (MN/m)	0.15	E (N/m^2)	2.1×10^{11}	C_{bz} (N s/m)	3.1×10^4
K_{cy} (MN/m)	0.15	GK (N m/rad)	1.9587×10^5	M_s (kg)	349
K_{cz} (MN/m)	0.4	K_{ry} (N/m)	2.947×10^7	M_b (kg/m)	466
K_{fx} (MN/m)	10	K_{rz} (N/m)	7.8×10^7	l_s(m)	0.6

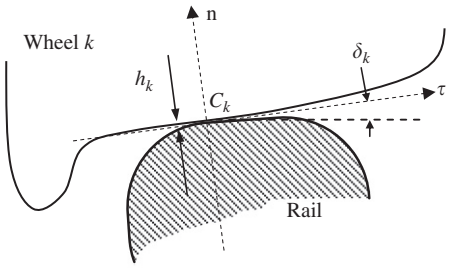

Fig. 7. Wheel k and rail in contact.

2.2.4. Calculation model of wheel–rail contact geometry

In order to carry out the rolling contact calculation of the wheel and rail with non-Hertzian rolling contact theory by Kalker [21], the normal distance and the contact angle of the wheel and rail, h_k and δ_k, as shown in Fig. 1 and also illustrated in Fig. 7, should be previously calculated. In Fig. 7, C_k is the contact point of the rail and wheel $k(=1$–$4)$, n and τ indicate, respectively, the normal and tangential directions at point C_k. These contact geometry parameters depend on Y_{wi}, ψ_{wi}, Y_{rk}, and the given profiles of the wheel and rail. Y_{wi}, ψ_{wi} and Y_{rk} are obtained through the dynamics calculation. In order to find the more accurate values of the contact geometry parameters, the method for the wheel–rail contact geometry analysis, discussed in Ref. [20], is further improved. In the contact geometry calculation using the improved method, C_k is directly searched according to the 3D geometry boundaries of the wheelset and the pair of rails, which are expressed with the numerical profile functions. The wheelset is set on or over the track for the given Y_{wi}, ψ_{wi} and Y_{rk}, and no penetration occurs between the wheel tread and the rail top. The rolling angle ϕ_{wi} of the wheelset is continuously changed in very small step size until the minimum vertical distances equal between the two wheels of the wheelset and the two rails. The points with the minimum vertical distance between them just form a pair of contact points of the wheel/rail, and indicated with C_k, as shown in Fig. 7. If C_k is found, h_k and δ_k are easily calculated.

2.3. Rolling contact theory of wheel and rail and material wear model

The normal pressure and the creepage between the wheel and rail determine the tangential traction, stick/slip areas, frictional work density and wear volume in the contact area, and the local deformation of the

wheel and rail under the condition that the profiles of the wheel and rail and the friction coefficient are given. Therefore, the two models, i.e., rolling contact mechanics model and material wear model, are very important in the numerical calculation of rail wear. Until now Kalker's rolling contact theory of 3D elastic bodies is very desirable in the rolling contact analysis of wheel and rail system in elastic region [20]. But, in using Kalker's theory for the analysis of the wheel and rail in rolling contact, the theory needs to be slightly modified. It was explained in Ref. [20].

The material wear model, in which material loss mass of unit area is proportional to frictional work of unit area [22,23], is introduced in the calculation of wear volume on the rail running surface. The friction coefficient and material physical properties of the wheel and rail were given in Refs. [10,14,15].

3. Numerical results and discussions

3.1. Curving dynamics characters of vehicle and track

When a vehicle passes through a track the normal load and creepage of wheel and rail determine whether or not rail corrugation initiates and develops. The basic condition necessary for the initiation and development of rail uneven wear is one of the following combinations: the fluctuating normal load and the fluctuating creepage, the fluctuating normal load and the non-zero constant creepage, and the constant normal load and the fluctuating creepage. If the fluctuating frequency of the normal load and the creepage vary in a certain limited range, the uneven wear, caused by such a fluctuating normal load or creepage, finally forms the corrugation with several wavelengths at a certain curving speed according to the relationship among wavelength, frequency and speed. Therefore, the characters of possible rail corrugation formation can be predicted according to the variation of the normal load or the creepage along the track when the vehicle passes through the track.

Through the detailed dynamics analysis of the vehicle running through the curved track at 80 km/h, the dynamical behaviors of the vehicle and track are acquired. Figs. 8(a) and (b) illustrate the lateral displacements and the yaw angles of the wheelsets, respectively. It is obvious that the lateral displacement and yaw angle of wheelset 1 (the leading wheelset) is much different from those of wheelset 2 (the trailing wheelset). At the circle curve, the lateral displacements of wheelsets 1 and 2 are, respectively, about -12 and -6 mm, and their yaw angles are, respectively, about 0.4° and 0°. "Negative" indicates that the wheelsets approaches to the high rail. The lateral displacements and the yaw angles change quickly at the transition curves. This situation could lead to the contact vibrations of the wheels and the rails when the vehicle passes through the transition curves.

Wheels 1 and 3 run on the high rail of the curved track and wheels 2 and 4 on the low rail. Fig. 9 shows that the normal loads of the four wheels vary along the curved track. The normal loads of wheels 1 and 3 are higher than those of wheels 2 and 4, respectively, namely, the normal load of the wheel of each wheelset on the high rail is larger than that of its wheel on the low rail. This is called the phenomenon of wheelset loading reduction caused by the vehicle curving. Usually, such a phenomenon leads to severe damage and wear on high curved rails at railway sites. The too large reduction of wheelset loading will cause that one side wheel of the wheelset is out of contact with the rail, and derailment occurs. Also Fig. 9 shows that, at the transition curves, the normal loads oscillate fiercely.

Figs. 10–12 illustrate, respectively, the longitudinal creepages, the lateral creepages, and the spin creepages of the four wheels along the curved track. The amplitudes of the total creepages of wheels 1 and 2 are larger than those of wheels 3 and 4. This is because the lateral displacement and the yaw angle of the leading wheelset are much larger than those of the trailing wheelset. It is interesting that the longitudinal creepage of wheel 1 is near zero at the circle curve since its longitudinal slips caused by the concerned factors are almost canceled, as shown in Fig. 10. The factors include the radius difference of the instant rolling circles of wheelset 1, the curvature of the curved track, the turnover of the high rail under wheel 1, the rigid motion of wheelset 1, etc. The change of the longitudinal creepage of wheel 1 on the high rail from the negative to near zero when it enters the circle curve from the transition curve means that the leading wheelset represents a bad curving behavior. Decreasing the negative longitudinal creepage of the wheel on the high curved rail will decrease the longitudinal creep force on the wheel in forward direction, therefore, decrease the wheel ability to reduce the

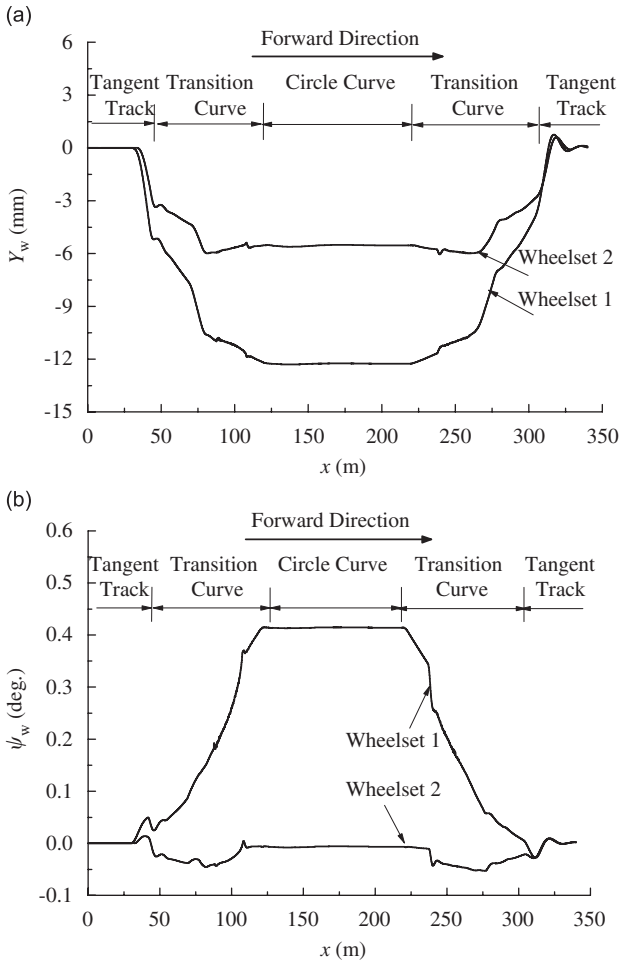

Fig. 8. (a) Lateral displacements of wheelsets and (b) yaw angles of wheelsets.

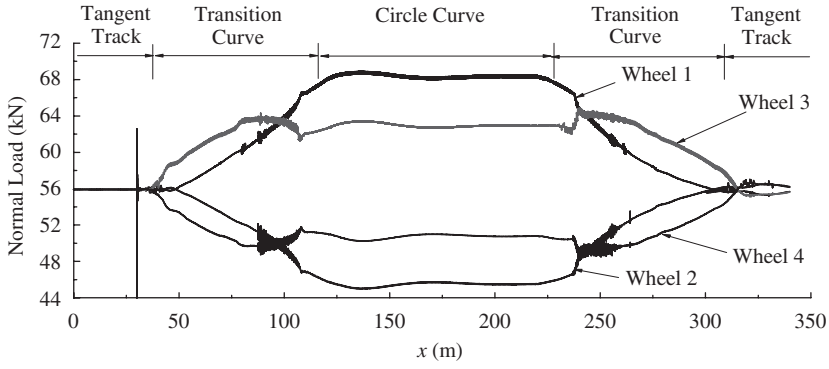

Fig. 9. Normal loads between rails and wheels.

attach angle (yaw angle) of the wheelset when the wheelset is curving. The further investigation into such a phenomenon is under way. Fig. 11 shows that the absolute value of the spin creepage of wheel 1 is the largest, compared to the other three wheels. This is because the lateral displacement of wheelset 1 is quite large, as

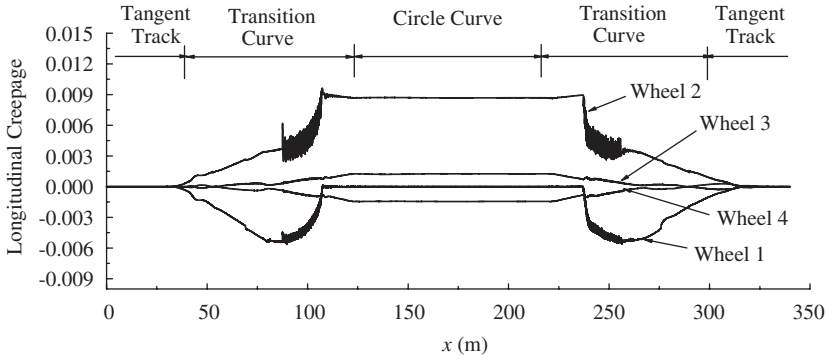

Fig. 10. Longitudinal creepages between rails and wheels.

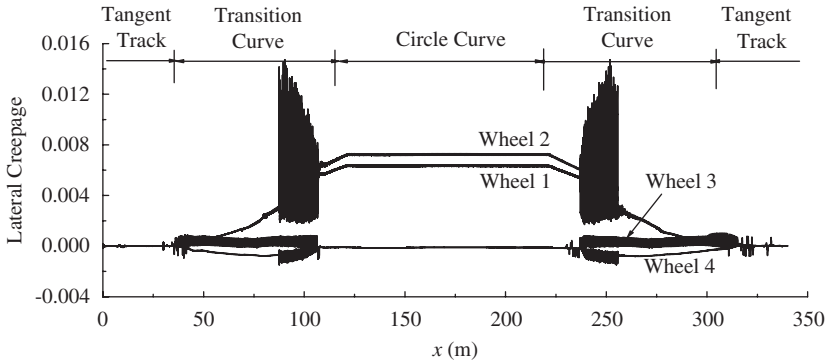

Fig. 11. Lateral creepages between rails and wheels.

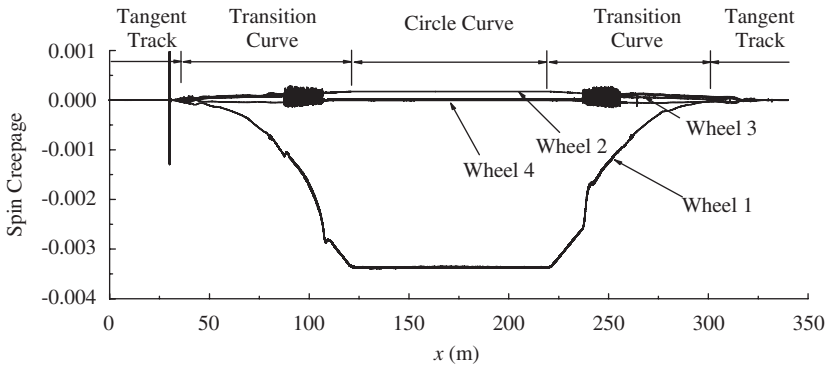

Fig. 12. Spin creepages between rails and wheels.

shown in Fig. 8(a), and the flange action of wheel 1 occurs. In such a situation the contact angle between wheel 1 and the high curved rail is very large, which causes the large spin creepage.

Figs. 10–12 also show the creepages of the wheels oscillate fiercely at high frequencies at the transition curves near to the circle curve, in particular the creepages of wheels 1 and 2. In order to clarify the frequency components of the oscillating the local curves of the normal loads and the lateral creepages, as shown in Figs. 9 and 11, are enlarged. Figs. 13 and 14 indicate the enlargements of the normal loads and the lateral creepages from the coordinate of 90–93 m, respectively. The main oscillating frequency of the normal load and the lateral creepage of wheel 3 is the same as the passing frequency of the sleepers. The peaks of the normal

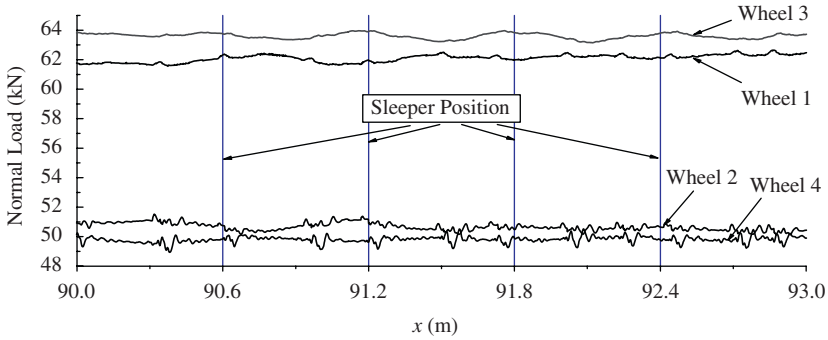

Fig. 13. Enlargement of the curves of the normal loads.

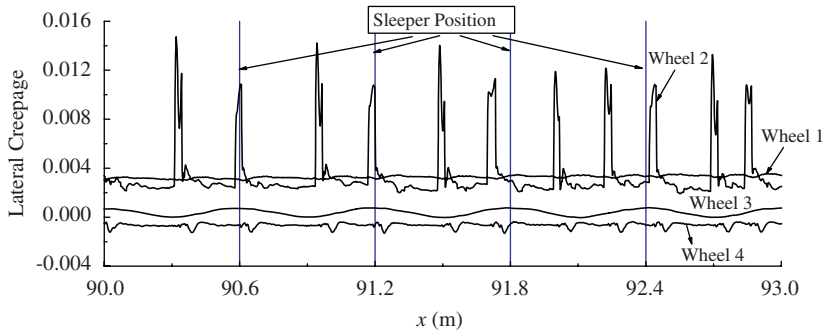

Fig. 14. Enlargement of the curves of the lateral creepages.

load and the lateral creepage of wheel 3 occur over the sleepers. The oscillating frequencies of the other three wheels comprise the higher frequencies than the passing frequency of the sleepers. These frequencies are the excited natural frequencies of the track. The frequencies will be further investigated in frequency domain.

Figs. 15(a) and (b) illustrate the linear spectrums of the normal loads of wheels 1–4. The thick solid lines in the figures denote the results of wheels 1 and 3, and the thin lines with circle signs for the results of wheels 2 and 4. It is obvious that the linear spectrums of the normal loads of the four wheels have a high peak at point A where is about 37 Hz. This frequency is the passing frequency of the sleepers. The track discrete support by the sleepers plays an important role in the fluctuating of the normal loads. Comparing wheel 1 with wheel 2, the oscillating components of their normal loads are nearly the same when the frequency is less than 350 Hz. When the frequency is larger than 350 Hz the normal load fluctuating of wheel 2 is stronger than that of wheel 1, particularly at points F, G, and H, where the frequencies are, respectively, about 440, 600, and 800 Hz. Comparing the result of wheel 3 with that of wheel 4 shown in Fig. 15(b), it is found that the oscillating of the normal load of wheel 4 is stronger than that of wheel 3 when the frequency is larger than about 100 Hz. However, the sleeper passing frequency of 37 Hz and the frequency of about 80 Hz play a key role in the fluctuating of the normal load of wheel 3, as at points A and B shown in Fig. 15(b). At around 8 Hz there is another peak present in the linear spectrums due to the excited resonant frequency of the vehicle. The frequencies at peaks from A to H are listed in Table 2. According to the frequencies in Table 2 and the running speed of 80 km/h the corresponding oscillating wavelengths of the normal loads are also listed in Table 2. It is obvious that the lateral creepages of the four wheels have the similar characters, as shown in Fig. 14. However, these excited resonant frequencies and the corresponding wavelengths will change with the increasing of the passages and the continue change of the running surfaces of the rails due to wear.

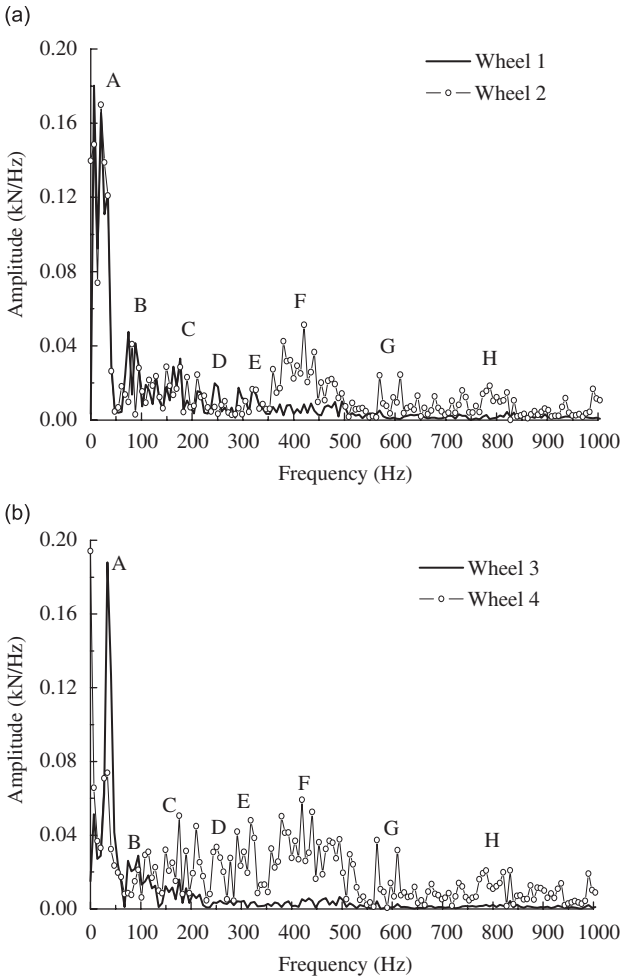

Fig. 15. (a) Linear spectrums of the normal loads of wheels 1 and 2 and (b) linear spectrums of the normal loads of wheels 3 and 4.

Table 2
Excited resonant frequencies and corresponding wavelengths

Points	A	B	C	D	E	F	G	H
Frequencies (Hz)	37	80	165	250	310	440	600	800
Wavelengths (mm)	600	278	135	89	71	50	37	28

3.2. Rail corrugations

3.2.1. Initiations of rail corrugations at different sections of a curved track

The initiations of rail corrugations at the different sections of the same curved track are analyzed at the same curving speed. The sections include the entering transition curve, the circle curve, and the exit transition curve, as shown in Fig. 16. In the sections the locations where the potential corrugation initiates are marked by ellipses of dash line border A–C. It is 30 m from ellipses A and C to their adjacent end of the circle curve, and ellipse B is at the center of the circle curve. The calculation length of calculated rail corrugation along the rail running surface is 3 m. It is noted that Figs. 13 and 14 indicate, respectively, the normal loads and the lateral creepages of the four wheels when the vehicle passes through the section marked by ellipse A. The normal loads and the creepages, when the vehicle passes through ellipses B and C, are not shown in the paper.

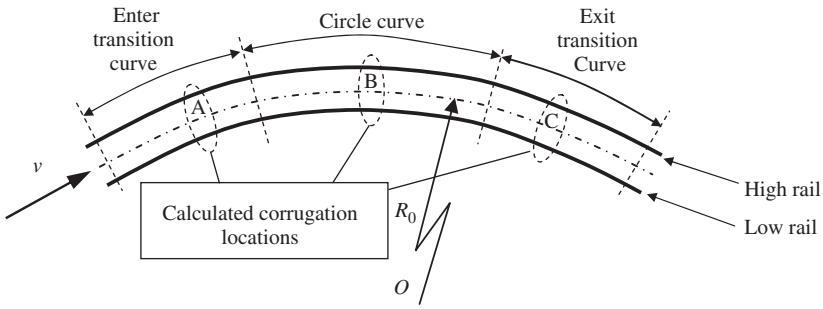

Fig. 16. Location of calculated rail corrugation on the curved track.

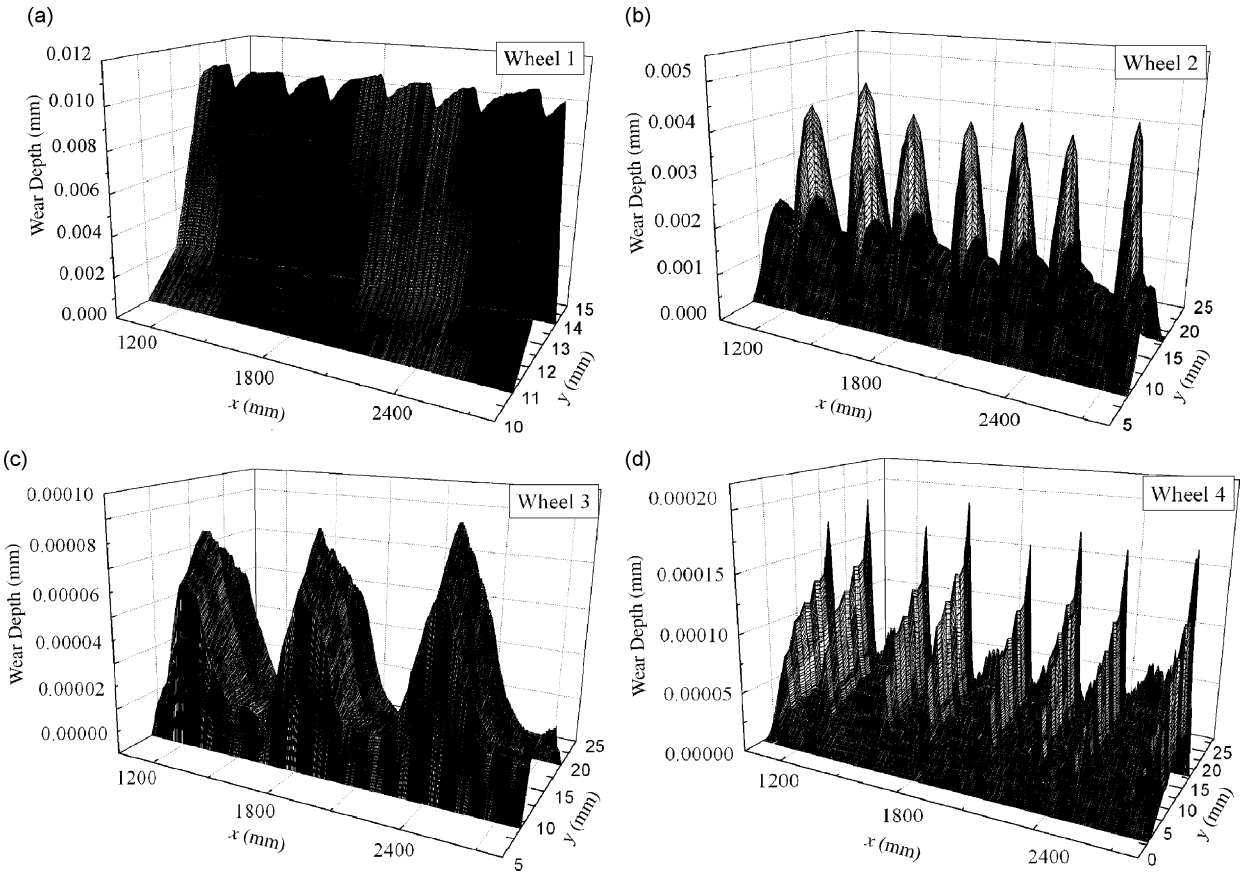

Fig. 17. Wear volumes by caused by wheels: (a) wheel 1, (b) wheel 2, (c) wheel 3, and (d) wheel 4.

Figs. 17(a)–(d) illustrate the initial rail corrugations caused by wheels 1–4, respectively, on the track section marked by ellipse A. When the vehicle passes over ellipse A there is a great difference between the wear volumes, the wavelengths of undulatory wear, and the ratios of the trough depth to the average wear depth caused by the wheels of the same bogie. The maximum wear depth caused by wheel 1 is about 2.5 times, 120 times, and 50 times of those by wheels 2–4, respectively. But the ratios of the uneven wear depth to the average wear depth caused by wheels 2–4 are much higher than that by wheel 1.

The present paper mainly concerns uneven wear depth forming on the rail running surface since the uneven wear leads to the strong vibration and noise generation of vehicle and track, and the use life reduction and damage of the parts. Fig. 18 illustrates the depths of the initial uneven wears caused by the four wheels, which equals to be the total wear depth reduced by the average wear depth. The initial uneven wear depth caused by

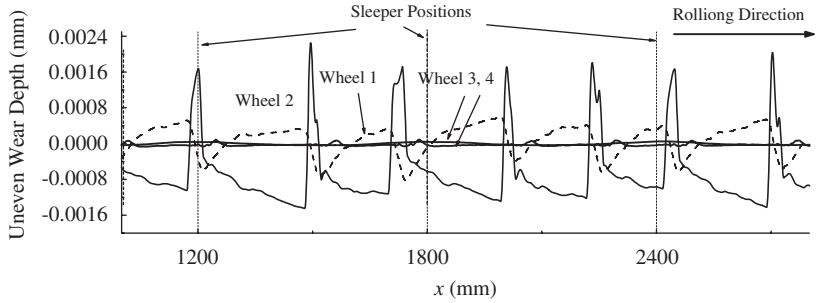

Fig. 18. Uneven wears caused by wheels at ellipse A.

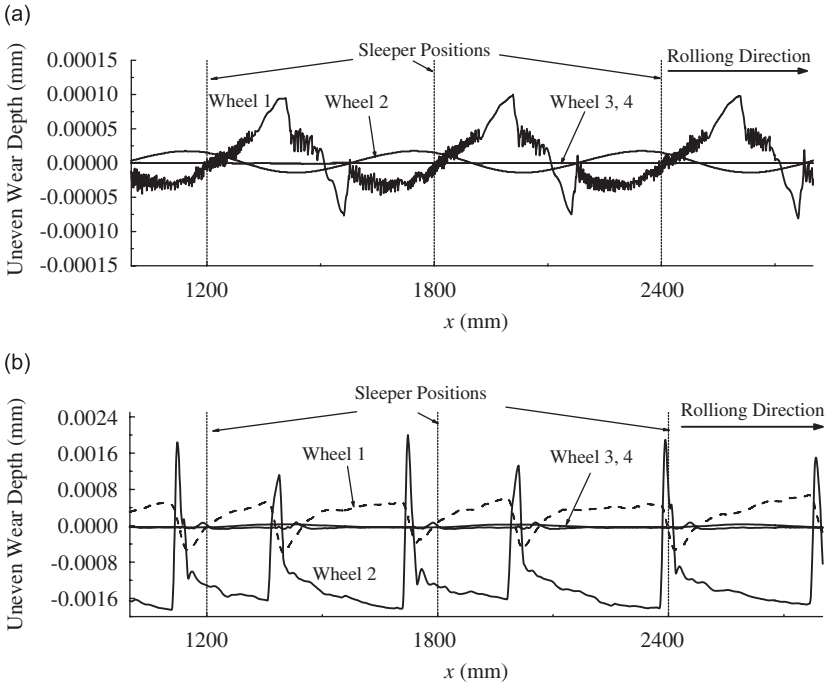

Fig. 19. (a) Uneven wears caused wheels at ellipse B and (b) at ellipse C.

wheel 2 is the largest, and that by wheel 1 follows the largest. The wavelengths of the initial corrugations caused by wheels 1 and 2 are almost consistent, and their main wavelengths vary from 220 to 290 mm. The troughs and crests of the corrugation caused by wheel 1 are opposite to those of the corrugation by wheel 2, as shown in Fig. 19, namely, there is the phase angle difference of about 180° between the corrugations caused by wheel 1 and wheel 2, which roll over the high rail and low rail, respectively. Such corrugations lead to the roll vibration of the vehicle at relatively high frequencies. The main wavelength of the corrugation caused by wheel 3 is 600 mm that is the passing frequency of the sleepers, as shown in Fig. 17(c). The main wavelengths of the initial corrugation caused by wheel 4 are the same as those of the initial corrugation caused by wheels 1 and 2, but their phases are different.

Figs. 19(a) and (b) indicate the uneven wears caused by the four wheels when the vehicle passes over the sections marked with ellipses B and C, respectively. Comparing Fig. 18 with Fig. 19, it is found that the initial corrugations on the entering transition curve resemble those on the exit transition curve. However, their crests and troughs with respect to the sleepers are different. The troughs of the initial corrugations caused by wheels 1 and 2 are much deeper than those caused by wheels 3 and 4. The initial corrugations represent 600 mm wavelength, which is related to the action of the discrete rail support by the sleepers. Especially when the vehicle passes through the track section of ellipse B (the circle curve) the normal loads of wheels 1 and 2, and

the displacements of the rails under wheels 1 and 2 oscillate at the passing frequency of the sleepers, which causes the initial corrugations with the passing frequency of the sleepers, as shown in Fig. 19(a). Fig. 19(a) shows the trough depth of the initial corrugation caused by wheel 1 is the largest, and that caused by wheel 2 is less the largest. The wear peak caused by wheel 1 occurs in the first half of each sleeper bay, the wear peak caused by wheel 2 in the second half of each sleeper bay, near to the sleeper. The phase between the wear peaks caused by wheels 1 and 2 is different, which readily leads to the roll vibration of the vehicle. The spikes in the curve for wheel 1 show that the undulatory wear oscillates with small amplitude and at higher frequencies due to the high-frequency oscillating of the normal load. The wavelength is around 10–12 mm. This oscillation is a sort of tone burst of tone burst. But, under the present analysis conditions wheels 3 and 4 don't cause the initial rail corrugation when the vehicle passes through the circle curve, in particular at ellipse B. Fig. 19(b) illustrates the depths of the uneven wears caused by the four wheels when the vehicle passes through ellipse C on the exit transition curve, as shown in Fig. 16. Comparing Fig. 18 with Fig. 19(b), the characters of the initial corrugations caused by the four wheels when the vehicle passes through ellipse A on the entering transition curve are similar to those when the vehicle passes through ellipse C on the exit transition curve.

3.2.2. Development of initial corrugation

When a vehicle passes through a track with initial corrugations which are related to the easily excited nature frequencies of the track, the initial corrugations develop quickly with the increasing of the vehicle passages. For simplicity, the present paper only discusses the development of the initial corrugations caused by the four wheels at ellipse A of the curved track. Fig. 20 illustrates that the maximum wear depths caused by the wheels of the same bogie at ellipse A grow with the passage increasing. In Fig. 20 curves 1, 2, 3, 4 and 5 indicate the wheel passages of 1, 5, 10, 20 and 30, respectively. Figs. 20(a)–(d) indicate the results for wheels 1–4, respectively. The main wavelengths of the growing corrugation caused by wheel 1 are the same as those caused by wheel 2. But the shorter wavelengths, which are from 30 to 80 mm, gradually appear in the developing corrugation caused by wheel 2 with the increasing of the passages. The passing frequency of the growing corrugation caused by the repeated passages of wheel 3 is the exactly same passing frequency of the sleepers, and the corrugation in development has a little tendency to move forward, as shown in Fig. 20(c). Fig. 20(d) represents not only the long wavelengths, which are the same as those of the corrugations caused by wheels 1 and 2, but also the short wavelengths ranging from about 28 to 130 mm, which are about the wavelengths listed in Table 2. The short wavelength corrugations grow quickly with the increasing of the passages, as shown in Fig. 20(d). There are sharp peaks in Figs. 20(b) and (d), which indicates that wheels 2 and 4 cause the formation of chasms on the low rail running surface of the curved track. The formation of the chasms is related to the characteristic oscillation of the lateral creepages of wheels 2 and 4, as shown in Fig. 14. The chasms on the rail running surface can cause the strong contact vibration between the wheel and rail.

It should be noted that Fig. 20 show the maximum wear depths after the vehicle passages of 30 which seem to be unrealistic. It is because the material wear model used in the calculation neglected the effect of repeated loading on the rail running surface on material work hardening. In addition, the present calculation considered the same type of vehicle with the same axle load and the same curving speed only. The wheel/rail contact traces on the rail top are not much different under the condition of different passages. The locations of wear calculation on the rail top are centralized in the transverse direction of the rail. Actually, the vehicles pass through a curved track every day and night, and their axle loads and curving speeds are different. The wheel/rail contact traces on the rail top are extensively distributed in the transverse direction and the wear is extensively distributed on the rail top. Hence, the actual wear depth should be less than the present numerical results as shown in Fig. 20. However, Fig. 20 reasonably shows the difference between the depths and characters of the corrugations caused by the four wheels of the same bogie.

Fig. 21 shows the wear volumes caused by the four wheels of the same bogie after the 30 passages of the vehicle through ellipse A on the entering transition curve. Figs. 21(a)–(d) indicate the results for wheels 1–4, respectively. The average wear volume caused by wheel 1 for each passage is the largest, compared to the other three wheels. It should be noted that the amplitudes of the corrugations caused by wheels 2–4 increase quickly

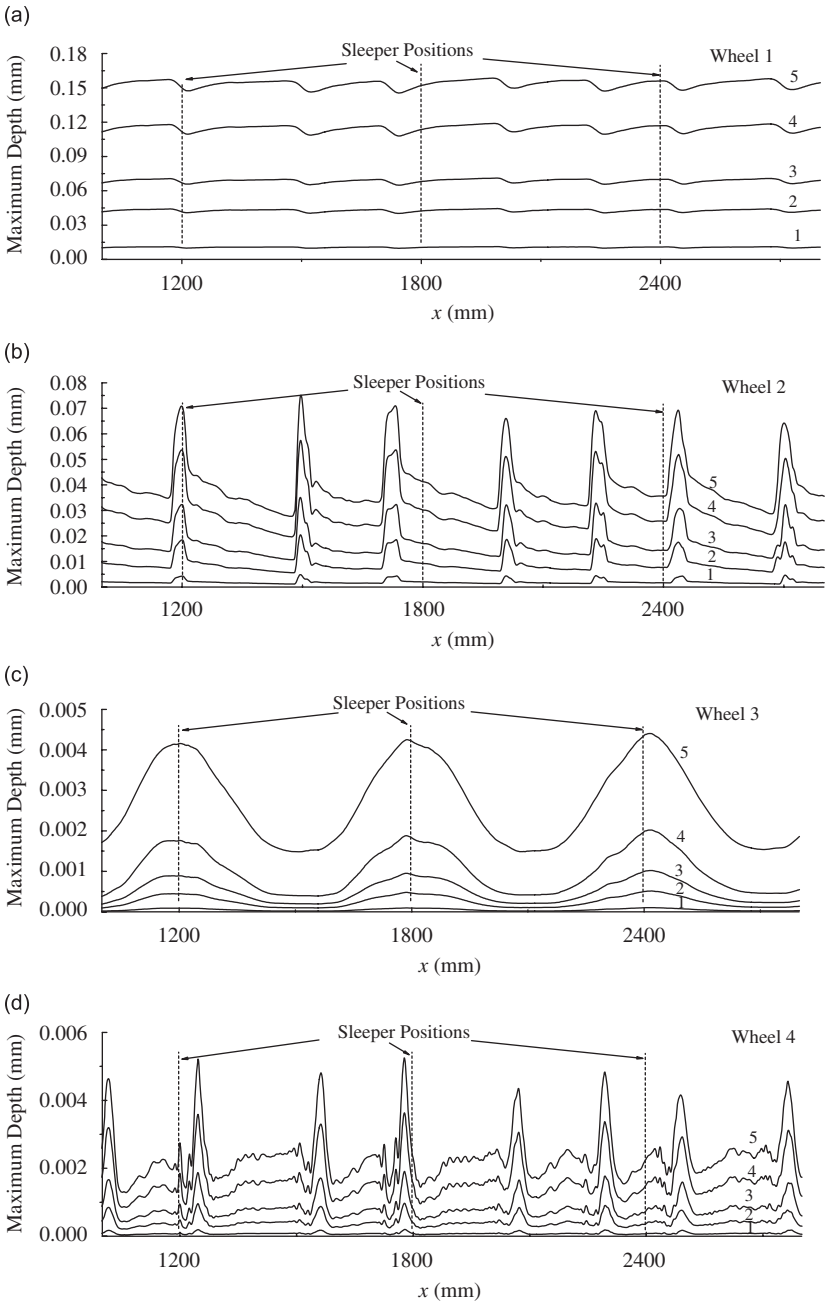

Fig. 20. Maximum wear depths caused by the four wheels after different passages.

with the passages increasing, in particular the amplitudes of the short wavelength corrugations caused by wheels 2 and 4 on the low rail grow fast. The wavelengths of the short corrugations range from 28 to 130 mm. But these surface plots can't present such short wavelengths clearly.

The characters and growth ratio of the corrugations occurring on the exit transition curve are similar to those on the entering transition curve. The passing frequencies of the corrugations occurring on the circle curve are almost the same as the passing frequency of the sleepers, and their growth is relatively low, compared to those on the transition curves. The results regarding the circle curve are not shown in the paper. After the further increasing of the passages, the corrugations on the transition curves develop and extend

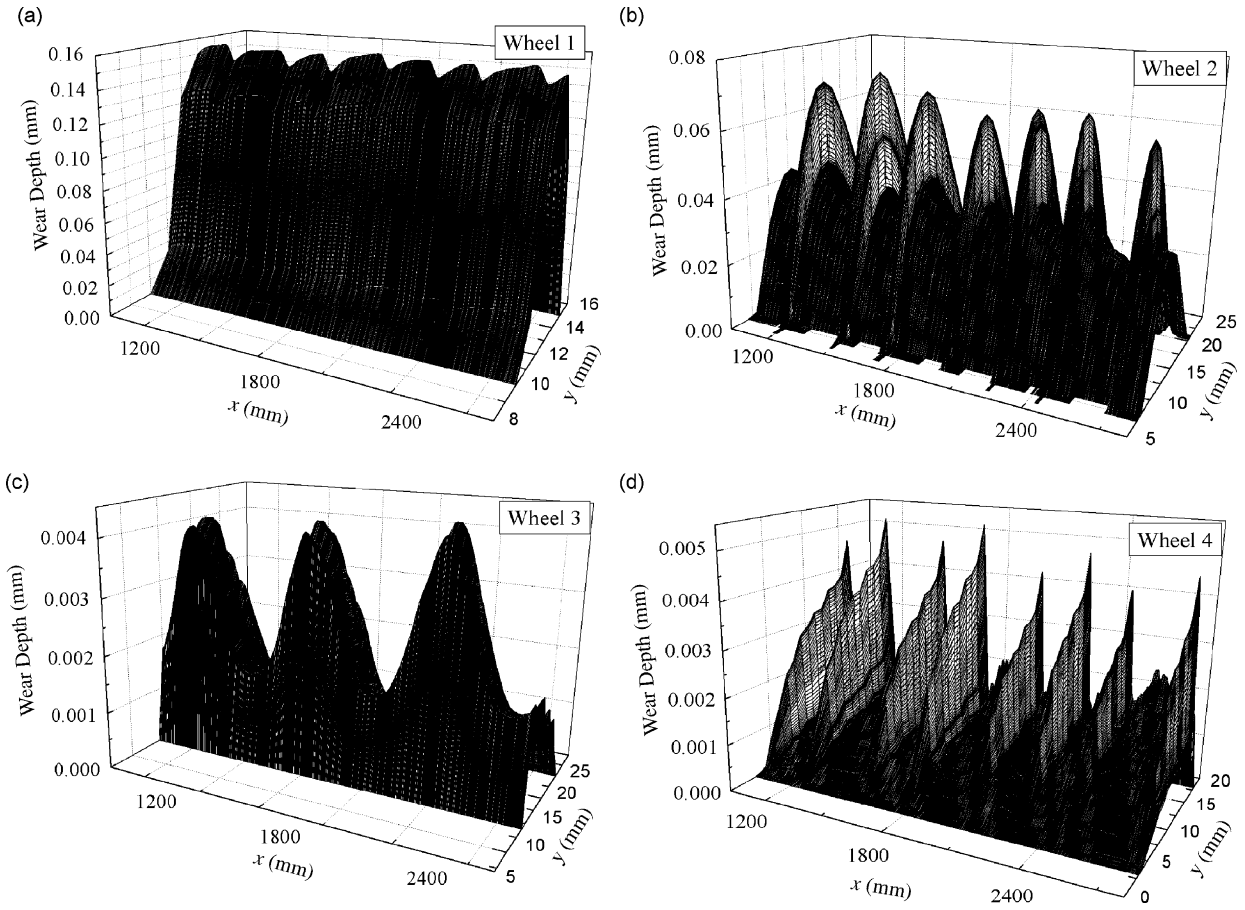

Fig. 21. (a) Wear volume caused by wheel 1, (b) by wheel 2, (c) by wheel 3, and (d) by wheel 4.

along the curved track and further to the neighboring tangent tracks. Finally, the corrugations formed on the whole curved track present very similar pattern.

It should be noted that in the present calculation no irregularities are introduced into the calculation model. Actually, a variety of potential irregularities, such as track geometry irregularities due to track construction, rail manufacturing, the damages and deformations of the rail after use, always exist on the curved track. The formation of corrugations on the curved track should be attributed to the combination of the variety of possible causes, which is further investigated in the near future. However, to date, it is very difficult to verify the present model of curved rail corrugation through a test in a laboratory or at a railway site. This is because, so far, any test facility cannot characterize the dynamic behavior of ballast tracks with discrete support by sleepers very well.

4. Conclusions

The present work investigates into the effect of discrete track support by sleepers on the initiation and development of rail corrugation at a curved track when a railway vehicle passes through the curved track using a numerical method. The numerical method considers a combination of Kalker's rolling contact theory with non-Hertzian form, a linear frictional work model and a dynamics model of a half railway vehicle coupled with the track. The track model is further improved to consider the effect of the rail discrete support motion with respect to the running vehicle, and also the calculation model of the fastening system is improved. The numerical analysis examines in detail the variations of wheel/rail normal loads, the creepages, and the rail

wear volume at the different sections of a same curved track. According to the obtained numerical results the conclusions are drawn as follows:

(1) It is found that the discrete rail support by sleepers causes the contact vibration of wheels and rails when a railway vehicle passes through a curved track. The normal loads and creepages of the wheels and rails oscillate at different frequencies. These frequencies include the passing frequencies of the track sleepers and the high excited track resonant frequencies. Therefore, rail corrugations initiate and develop with several wavelengths.
(2) The patterns of rail corrugations caused by the wheels of a same bogie are different when it passes through a curved track. The wear volume on the high curved rail caused by wheel 1 is the largest due to the large normal loads and the large creepages between wheel 1 and the high curved rail, compared with the other three wheels. However, the amplitudes of the corrugations caused by wheels 2–4 increase more quickly than that by wheel 1 on the high rail with the increasing of the vehicle passages. The main long wavelengths of the corrugations caused by wheels 1, 2, and 4 are not much different. The corrugation caused by wheel 3 presents only one wavelength which is the same as the sleeper pitch. Also the corrugations caused by wheels 2 and 4 characterize the short wavelengths varying from about 28 to 130 mm. Also the wave-depths of the uneven wears with such short wavelengths increase quickly with the increasing of the passages.
(3) Compared to the situation of the uneven wear on the circle curve, the rail corrugation readily initiates and quickly develops on the transition curve.

Acknowledgements

This project is supported by the National Natural Science Foundation of China (no. 50521503), the National Basic Research Program of China (973 Program, no. 2007CB714702) and FANEDD (no. 200248).

The authors are grateful to thank the reviewers for their valuable technical advice and their kind help in improving the English text of the paper.

References

[1] R.A. Clark, Slip–stick vibrations may hold the key to corrugation puzzle, *Railway Gazette International* 17 (1984) 531–533.
[2] R.A. Clark, P.A. Dean, J.A. Elkins, S.G. Newton, An investigation into the dynamic effects of railway vehicles running on corrugated rails, *Journal of Mechanical Engineering Science* 24 (1982) 65–76.
[3] C.R. Brockly, The influence of track support structure and locomotive traction characteristics on short wavelength corrugations, *Wear* 153 (1992) 315–322.
[4] S.L. Grassie, J. Kalousek, Rail corrugation: characteristics, cause and treatments, *Proceedings of the Institution of Mechanical Engineers* 207 (Part F) (1993) 57–68.
[5] D.K. Ahlbeck, L.E. Daniels, A review of rail corrugation processes under different operating modes, *Proceedings of the ASME Joint Railroad Conference*, 1990, pp. 13–18.
[6] K. Knothe, B. Ripke, The effects of parameters of wheelset, tract and running conditions on the growth rate of rail corrugation, *VSD (Supplement)* 18 (1989) 345–356.
[7] K. Hempelmann, K. Knothe, An extended linear model for the prediction of short pitch corrugation, *Wear* 191 (1996) 161–169.
[8] E.G. Vadillo, J.A. Tarrago, G.G. Zubiaurre, C.A. Duque, Effect of sleeper distance on rail corrugation, *Wear* 217 (1998) 140–146.
[9] I. Gomez, E.G. Vadillo, An analytical approach to study a special case of booted sleeper track rail corrugation, *Wear* 251 (2001) 916–924.
[10] X.S. Jin, Z.F. Wen, K.Y. Wang, Effect of track irregularities on initiation and evolution of rail corrugation, *Journal of Sound and Vibration* 285 (1–2) (2005) 121–148.
[11] T.X. Wu, D.J. Thompson, Vibration analysis of railway track with multiple wheels on the rail, *Journal of Sound and Vibration* 239 (2001) 69–97.
[12] T.X. Wu, D.J. Thompson, Behavior of the normal contact force under multiple wheel/rail interaction, *Vehicle System Dynamics* 37 (2002) 157–174.
[13] T.X. Wu, D.J. Thompson, An investigation into rail corrugation due to micro-slip under multiple wheel/rail interactions, *Wear* 258 (2005) 1115–1125.
[14] X.S. Jin, Z.F. Wen, K.Y. Wang, Z.R. Zhou, Q.Y. Liu, C.H. Li, Three-dimensional train–track model for study of rail corrugation, *Journal of Sound and Vibration* 293 (3–5) (2006) 830–855.

[15] X.S. Jin, Z.F. Wen, K.Y. Wang, X.X. Biao, Effect of passenger car curving on rail corrugation at a curved track, *Wear* 260 (2006) 619–633.
[16] A. Igeland, H. Ilias, Rail head corrugation growth predictions based on non-linear high frequency vehicle/track interaction, *Wear* 213 (1997) 90–97.
[17] C. Andersson, A. Johansson, Prediction of rail corrugation generated by three-dimensional wheel–rail interaction, *Wear* 257 (2004) 423–434.
[18] P.A. Meehan, W.J.T. Daniel, T. Camey, Prediction of the growth of wear-type rail corrugation, *Wear* 258 (2005) 1001–1013.
[19] X.S. Jin, X.X. Biao, Z.F. Wen, K.Y. Wang, Effect of sleeper pitch on rail corrugation at a tangent track in vehicle hunting, *Proceedings of the Seventh International Conference Contact mechanics and Wear of Rail/Wheel Systems*, Brisbane, Australia, September 24–26, 2006, pp. 179–188.
[20] X.S. Jin, Z.F. Wen, W.H. Zhang, Z.Y. Shen, Numerical simulation of rail corrugation on curved track, *Computers & Structures* 83 (2005) 2052–2065.
[21] J.J. Kalker, *Three-Dimensional Elastic Bodies in Rolling Contact*, Kluwer Academic Publishers, The Netherlands, 1990.
[22] P.J. Bolton, P. Clayton, I.J. McEwan, Rolling-sliding wear damage in rail and tyre steels, *Wear* 120 (1987) 145–165.
[23] P. Clayton, Tribological aspects of wheel–rail contact: a review of recent experimental research, *Wear* 191 (1996) 170–183.
[24] W.M. Zhai, C.B. Cai, S.Z. Guo, Coupling model of vertical and lateral vehicle/track interactions, *Vehicle System Dynamics* 26 (1996) 61–79.
[25] K.Y. Wang, W.M. Zhai, C.B. Cai, The model of locomotive-track spatially coupled dynamics and its verification, *Journal of China Railway Society* 24 (4) (2002) 21–27 (in Chinese).
[26] Z.Y. Shen, J.K. Hedrick, J.A. Elkins, A comparison of alternative creep-force models for rail vehicle dynamic analysis, *Proceedings of the Eighth IAVSD Symposium*, Cambridge, MA, USA, 1983, pp. 591–605.
[27] J.J. Kalker, On the Rolling Contact of Two Elastic Bodies in the Presence of Dry Friction, PhD Thesis, Delft University, The Netherlands, 1967.
[28] J.K. Vermulen, K.L. Johnson, Contact of non-spherical bodies transmitting tangential forces, *Journal of Applied Mechanics* 31 (1964) 338–340.
[29] W.M. Zhai, C.B. Cai, Q.C. Wang, Z.W. Lu, X.S. Wu, Dynamic effects of vehicle on track in the case of raising train speeds, *Proceedings of the Institution of Mechanical Engineers* 215 (Part F) (2001) 125–135.
[30] K.Y. Wang, W.M. Zhai, TTISIM Software for vehicle–track coupling dynamics simulation and its verification, *China Railway Science* 25 (6) (2004) 48–53 (in Chinese).